An Overall System Delay Compensation Method for IPMSM Sensorless Drives in Rail Transit Applications

Hang Zhang, *Student Member, IEEE*, Weiguo Liu, *Senior Member, IEEE*, Zhe Chen, and Ningfei Jiao, *Member, IEEE*

***Abstract*—In rail transit application, the multimode pulsewidth modulation (PWM) is used to take full advantage of the dc-bus voltage in wide speed range. To improve the sensorless control performance of interior permanent magnet synchronous motor (IPMSM) drives in this condition, an overall system delay compensation method is proposed for a hybrid position observer that combines a simple square-wave voltage injection with a nonsingular terminal sliding mode observer. Due to the delay effect, the currents and position estimation performance are deteriorated, such as more severe dq-axis currents coupling and fluctuation of estimated position error. In order to solve these problems, the analysis of delay characteristics in the IPMSM sensorless drives is first presented. For carrier-based modulation, the compensation time is obtained through a self-tuning PI regulator based on predictive q-axis voltage error. Then, the three-phase reference currents are utilized to judge the direction near zero-crossing point and the parameters robustness is also analyzed. For optimal PWM modulation, the voltage vector angle and modulation depth are predicted in a simple way, and the delay effect can be eliminated. Furthermore, the harmonics distribution in sensorless control is described by power spectral density. Finally, the effectiveness of proposed strategy is verified by experimental results with a 3.7-kW IPMSM sensorless drive platform.**

***Index Terms*—Hybrid sensorless control, interior permanent magnet synchronous motor (IPMSM), multimode pulsewidth modulation (PWM), nonsingular terminal sliding mode observer (NTSMO), overall system delay compensation, square-wave voltage injection (SWVI).**

I. Introduction

DIFFERENT from general industry applications, permanent magnet synchronous motor (PMSM) traction system often has two characteristics in rail transit: low switching frequency [1], and multimode pulsewidth modulation (PWM) [2].

Manuscript received January 16, 2020; revised June 13, 2020; accepted July 29, 2020. Date of publication August 11, 2020; date of current version September 22, 2020. This work was supported in part by the National Natural Science Foundation of China under Grant 51707161, in part by the Nature Science Basic Research Plan in Shaanxi Province of China under Grant 2018JQ5187, and in part by the Fundamental Research Funds for the Central Universities under Grant 3102020ZDHKY06. Recommended for publication by Associate Editor J.-I. Itoh. *(Corresponding author: Zhe Chen.)*

The authors are with the Shaanxi Key Laboratory of Small and Special Electrical Machine and Drive Technology, School of Automation, Northwestern Polytechnical University, Xi'an 710072, China (e-mail: wdvvv420@126.com; lwglll@nwpu.edu.cn; zhe.chen@nwpu.edu.cn; jiaoningfei@gmail.com).

Color versions of one or more of the figures in this article are available online at https://ieeexplore.ieee.org.

Digital Object Identifier 10.1109/TPEL.2020.3015742

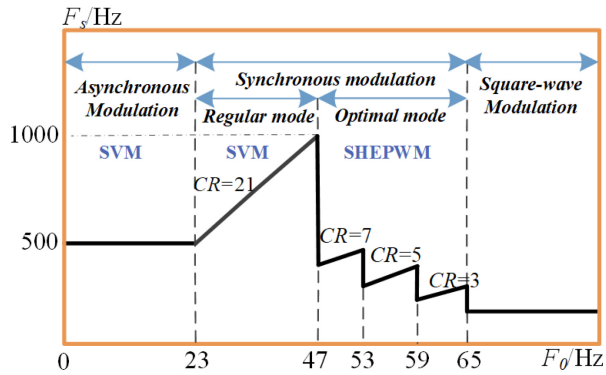

Fig. 1. Multimode PWM in rail transit application.

In order to have better symmetric performance of output three-phase currents, the PWM strategy adopts asynchronous space vector modulation (SVM) at low speed, segmented synchronous modulation at middle or high speed, as shown in Fig. 1, where F_s and F_0 are switching and fundamental frequency, respectively, $\mathrm{CR} = F_s/F_0$. In addition, for traction system, the fault of position sensor during operation results in potential risk, then the sensorless control strategy is essential for its reliability, which has been attracting attentions from both industry and academia [3]–[5]. Nowadays, in sensorless drives, the system delay effect cannot be neglected. Furthermore, the aforementioned two characteristics bring new challenges to system delay compensation, and its influence on position estimation performance is worth analyzing.

In electric traction drives, the system delay of vector closed-loop control mainly includes inverter nonlinearity delay [6], algorithm execution time, and sample filter delay. The latter factors can be summarized as calculation delay [7]. For the inverter nonlinearity delay effect in sensorless control, many scholars have analyzed its impact on high-frequency voltage injection (HFVI) [8]–[10] and back EMF model method [11], [12]. In HFVI, the induced HF current appears distortion in the case of inverter nonlinearity delay, which affects the extraction accuracy of the fundamental signal, then the speed and position estimation accuracy is also deteriorated. In [8], the influence of inverter nonlinearity delay on HFVI is first analyzed, and the condition that compensation strategy can effectively eliminate the injected voltage error is given. When using square-wave

voltage injection (SWVI), Kim *et al.* [9] describe the induced HF current distortion caused by inverter nonlinearity, then a voltage signal with amplitude variation is injected to correct the induced currents error. In [10], the ideal insulated gate bipolar transistor (IGBT) model under different operating conditions can be obtained by look-up table, and the model is used to compensate the voltage distortion caused by inverter nonlinearity, then the position estimation error is eliminated. On the other hand, the performance of back EMF based sensorless method is also affected by this inverter delay factor. Generally, the $\alpha\beta$-axis reference voltages instead of measured voltages are used for position estimation, the voltage error caused by the inverter nonlinearity should be compensated. An adaptive notch filter based on adaptive noise canceling principle combined with the EMF-based observer is proposed in [11], and the position estimation accuracy is improved. Liang *et al.* [12] propose an adaptive super-twisting algorithm based sliding-mode observer for surface-mounted PMSM sensorless control, in which voltage source inverter (VSI) nonlinearity is taken into consideration and the calculated voltage errors are compensated for U_d and U_q. As can be seen, the most existing inverter nonlinearity compensation methods in sensorless control are analyzed in asynchronous modulation, which is not the case of rail transit application. Because the inverter enters synchronous PWM modes as speed increases, the influence of dead time on voltage distortion also changes, and the sensorless performance needs to be further considered.

For the "one step delay" caused by the inherent digital system calculation, there are some literatures focusing on evaluating its influence on closed-loop performance of position observer. For HFVI, when the injected frequency is close to the switching frequency, the calculation delay cannot be neglected. Wang *et al.* [13] present a novel pseudorandom HF SWVI, and the power spectra density (PSD) performance in induced HF currents is optimized. By using a delay compensation method for signal demodulation, the position estimation error is reduced. In [14], a strategy to inject three HF pulsating voltages with different frequencies and amplitudes into ABC frame is proposed, meanwhile, a new signal processing strategy is developed to completely eliminate the effects of system delay. For the back EMF based strategies, based on q-axis current error, Zhang *et al.* [7] propose a global time-delay compensation, and the lag angle can be eliminated in position estimation process. In [15], to solve the problem of calculation delay caused by digital computation, a current precompensation scheme based on dual-sampling strategy in one switching period is proposed for sliding mode observer, then the accuracy of position estimation can be improved. In [16], for the high-speed PMSM sensorless control, a time delay model is used in estimation of back EMF, and the cross-coupling of dq-axis currents observer is obviously improved.

From aforementioned analysis, the existing compensation strategies eliminate either the effect of inverter nonlinearity or calculation delay under asynchronous modulation. However, the two delay effects in sensorless control are dependent on motor operation frequency [12]. Especially, for rail transit drive with segmented synchronous modulation, the harmonic components change greatly compared to the asynchronous SVM [17], the used optimal PWM is not a carrier-based way [18]. As a result, the performance of hybrid position observer under the combined delay action needs to be further discussed, and the design of a global system delay compensation is worth exploring. Generally, the hybrid position observer is a good solution to achieve whole-speed-range sensorless control, which uses HFVI in low speed and fundamental-model method in high speed [19]. Nowadays, many efforts also have been made to improve the performance of hybrid sensorless control from stability and dynamics in the transition zone [20], [21]. But it is not combined with time delay in multimode PWM.

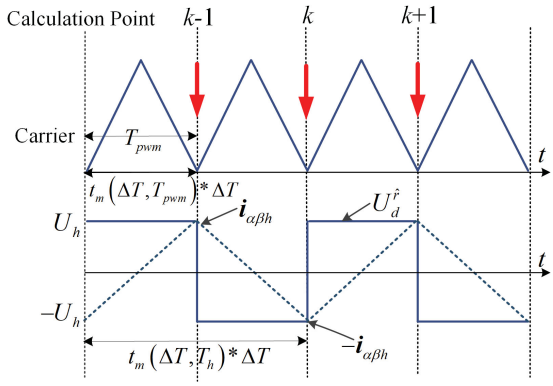

Fig. 2. Calculation sequence of square-wave injection.

In this article, an overall system delay compensation strategy is proposed for IPMSM hybrid sensorless drives under multimode PWM. A simple SWVI and nonsingular terminal sliding mode observer (NTSMO) are used in low- and high-speed region, respectively. The structure is organized as follows. Section II gives the principle of hybrid position observer design. The influence of system delay effect on sensorless performance is analyzed in Section III. According to the characteristics of different PWM modes, Section IV gives the implementation process of the proposed delay compensation in position estimation. The effectiveness of the delay-elimination-based sensorless control has been verified via experiments on a 3.7-kW IPMSM drive platform in Section V.

II. Principle of Hybrid Position Observer Design

A. Position Information Extraction

In low-speed region, when the square-wave voltage is injected to estimate the d-axis, the rotor position information that hides in envelops of $\alpha\beta$-axis HF currents can be decoded, as described in [22]. Here, a simple demodulation way is designed to avoid the phase lag caused by filters. In PWM generation, the output voltage pulse can be equivalent to the superposition of fundamental and high-frequency components. The induced $\alpha\beta$-axis currents also contain the same items, which can be expressed as

$$\boldsymbol{i}_{\alpha\beta} = \boldsymbol{i}_{\alpha\beta f} + \boldsymbol{i}_{\alpha\beta h} \tag{1}$$

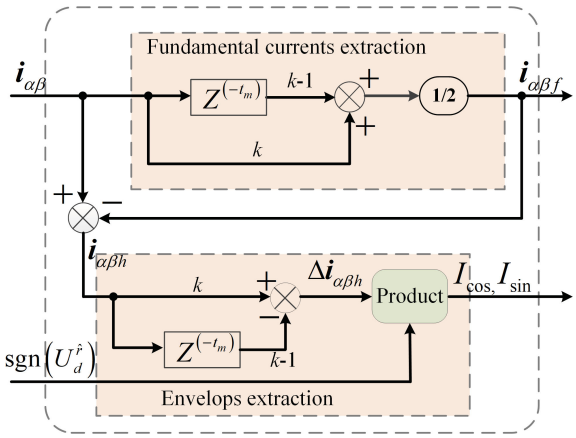

Fig. 3. Extraction of HF currents envelops.

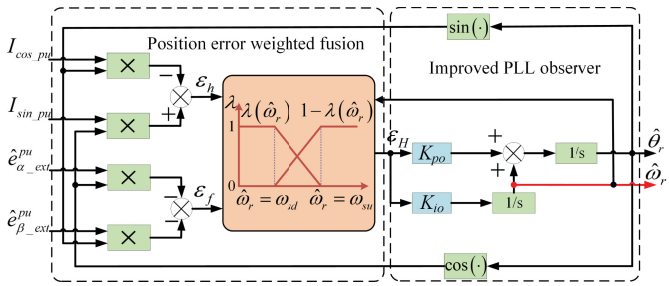

Fig. 4. Structure of hybrid position observer.

where subscripts f and h represent the fundamental and high-frequency components, respectively. Fig. 2 shows the calculation sequence of SWVI, T_{pwm} is carrier period, ΔT is current sampling interval, t_m is integer multiple of a specific period relative to ΔT, $U_d^{\hat{r}}$ is injected square-wave signal, and T_h is injected cycle. Based on this condition, the fundamental current does not change during the time interval from $k-1$ to k, and the following relationship can be obtained

$$\begin{cases} \boldsymbol{i}_{\alpha\beta}(k-1) = \boldsymbol{i}_{\alpha\beta f} + \boldsymbol{i}_{\alpha\beta h} \\ \boldsymbol{i}_{\alpha\beta}(k) = \boldsymbol{i}_{\alpha\beta f} - \boldsymbol{i}_{\alpha\beta h}. \end{cases} \tag{2}$$

By adding $\boldsymbol{i}_{\alpha\beta}(k-1)$ and $\boldsymbol{i}_{\alpha\beta}(k)$, the fundamental feedback current can be obtained without using low-pass filter (LPF), then a simple envelops extraction method can be designed, as shown in Fig. 3, $I_{\cos}$ and $I_{\sin}$ are envelops of α- and β-axis HF current, respectively. As the speed increases, the back EMF reaches the detectable point, then NTSMO in [7] is used, and the estimated $\alpha\beta$-axis back EMF can be obtained to construct phase-locked loop (PLL) position observer.

B. Position Observer Design and Parameters Analysis

Fig. 4 shows the implementation process of hybrid position observer, where pu in subscript or superscript represents the standardized value, $I_{\cos\_pu}$ and $I_{\sin\_pu}$ are envelops signal in SWVI, $\hat{e}^{pu}_{\alpha\_\text{ext}}$ and $\hat{e}^{pu}_{\alpha\_\text{ext}}$ are estimated back EMF in NTSMO, ε_H is input hybrid position error, and ω_{sd} and ω_{su} are the upper and low limit of speed in transition zone, respectively. In the weighting process, the input hybrid position error satisfies $\varepsilon_H = \lambda\varepsilon_h + (1-\lambda)\varepsilon_f$, λ is weighting factor, and can be calculated by the slope in Fig. 4. For the PLL parameters, through cross-multiplication calculation, ε_H can be equivalent to $\sin(\theta_r - \hat{\theta}_r)$. When the estimated value approaches the real position, the following relationship can be obtained:

$$\begin{cases} \dot{\hat{\omega}}_r = K_{io}\left(\theta_r - \hat{\theta}_r\right) \\ \dot{\hat{\theta}}_r = \hat{\omega}_r + K_{po}\left(\theta_r - \hat{\theta}_r\right). \end{cases} \tag{3}$$

Then, the transfer function between θ_r and $\hat{\theta}_r$ can be shown as

$$\frac{\hat{\theta}_r(s)}{\theta_r(s)} = \frac{K_{po}s + K_{io}}{s^2 + K_{po}s + K_{io}}. \tag{4}$$

If the two negative real poles of the characteristic equation $s^2 + K_{po}s + K_{io}$ are coincident with $-\rho$, then $K_{io} = \rho^2$, $K_{po} = \rho$, and the PLL stability can be guaranteed. Combined with the actual speed change, through (3), the parameters can be calculated as follows:

$$R_\omega / \sin\left(\tilde{\theta}_{re\_\max}\right) = \rho^2 \tag{5}$$

where $\tilde{\theta}_{re\_\max}$ is maximum expected error of estimated rotor position and R_ω is speed change rate.

III. Influence of System Delay on Sensorless Performance

A. Basic System Delay Effect

When the fundamental speed is low, the duty ratio (DR) is small, and the inverter nonlinearity delay causes distortion of the output voltage. At this time, the inherent calculation delay effect is not obvious. In high-speed region, DR gradually increases, and the control error caused by calculation delay makes the coupling degree of dq-axis currents more serious. Especially under low switching frequency, this delay effect is more pronounced.

First, influence of inverter nonlinearity delay is analyzed, and Fig. 5 shows the relationship comparison between A-phase ideal- and actual-inverter output voltages, where T_{pwm} is switching period and n is period index. For the three-phase two-level inverter circuit, the characteristics of each leg are same. Here, the A-phase is selected to demonstrate the inverter nonlinearity delay effect. Taking $i_A > 0$ in speed-fall process as an example, as can be seen, due to dead time T_{dead}, the actual A-phase voltage becomes U_{AN_1}. Furthermore, due to the existence of turn-ON time T_{on} and turn-OFF time T_{off}, the actual voltage becomes U_{AN_2}. U_{err} is the inverter output voltage error and satisfies $U_{\text{err}} = U_{AN}^{\text{ideal}} - U_{AN\_2}$, in this condition, the compensation time is $T_{\text{dead}} + T_{\text{on}} - T_{\text{off}}$. For $i_A < 0$, the compensation time is $T_{\text{off}} - T_{\text{dead}} - T_{\text{on}}$. Obviously, when using asynchronous SVM in Fig. 6(a), $T_{\text{pwm}}(n) = T_{\text{pwm}}(n+1)$, the output voltage errors of two adjacent switching periods are the same. In Fig. 6(b), when using synchronous SVM, $T_{\text{pwm}}(n+1) > T_{\text{pwm}}(n)$, and in speed-rise, $T_{\text{pwm}}(n+1) < T_{\text{pwm}}(n)$. Through the comparison, in same dynamic state condition, the voltage errors U_{err} are different. It means that the inverter nonlinearity delay compensation

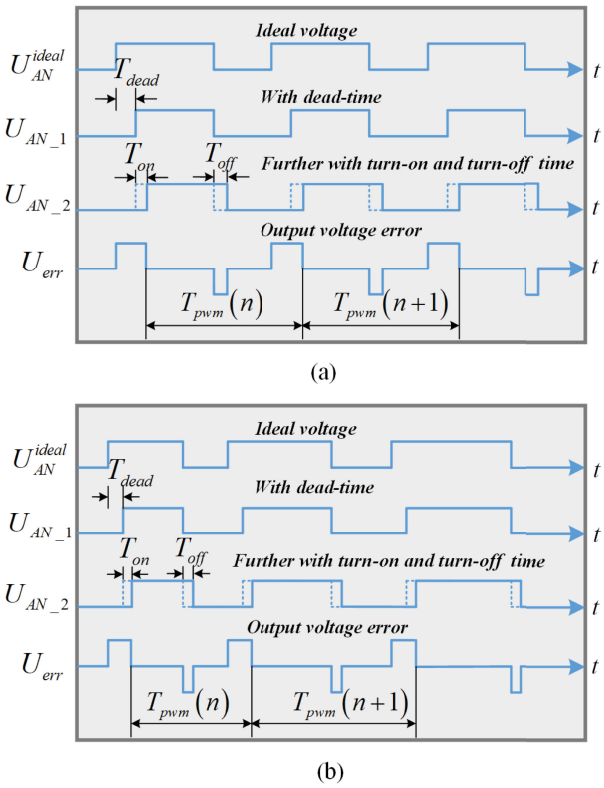

Fig. 5. Relationship comparison between A-phase ideal and actual output voltages for $i_A > 0$ in speed-fall process when considering inverter nonlinearity delay. (a) Asynchronous SVM. (b) Synchronous SVM.

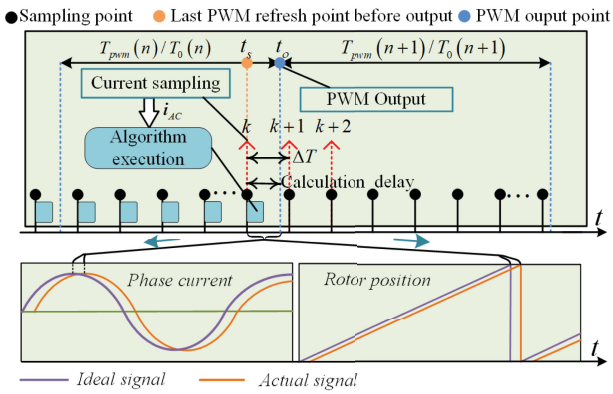

Fig. 6. Influence of inherent calculation delay.

needs to consider the difference. If the ON-voltages of IGBT and freewheeling diode both are neglected, the distorted voltage magnitude can be expressed as

$$U_{\mathrm{err}}(n) = \frac{T_{\mathrm{dead}} + T_{\mathrm{on}} - T_{\mathrm{off}}}{T_{\mathrm{pwm}}(n)} U_{\mathrm{dc}} \tag{6}$$

where U_{dc} is dc voltage, and the voltage error caused by the inverter nonlinearity delay varies with the switching frequency.

As described in [23], with asynchronous SVM, the voltage error in (6) causes $(6k \pm 1)$th harmonics in excited currents. Through coordinate transformation, sixth pulsation component

TABLE I
SYSTEM DELAY TIME CHARACTERISTICS

Parameters	Value$[Unit]$
Dead Time	$25[\mu s]$
IGBT turn-on time	$1[\mu s]$
IGBT turn-off time	$2.5[\mu s]$
Algorithm execution time	$150[\mu s]$
Control period	$200[\mu s]$

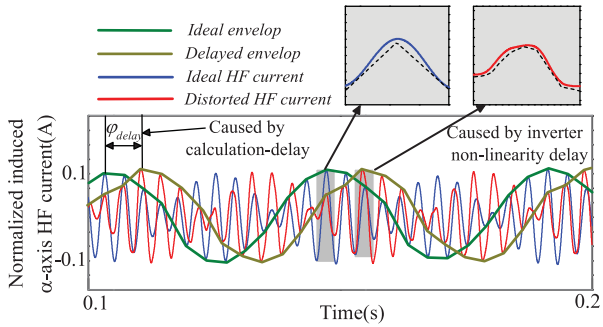

Fig. 7. Influence of system delay on SWVI.

appears in the dq-axis currents, that is, the inverter nonlinearity delay effect can be reflected by the magnitude of fifth and seventh harmonics in phase currents or $\alpha\beta$-axis currents.

Second, when the motor operates in high-speed region, especially in the SHEPWM mode, the pulse form gradually approaches the single pulse mode, the inverter nonlinearity delay is negligible relative to the operation time of effective voltage-vector during a switching cycle. Fig. 6 shows the influence of calculation delay on the closed-loop system, where T_0 is fundamental voltage period, t_o is PWM output time, and t_s is the last sampling time before PWM output. Obviously, according to the period relationship, $t_o - t_s \leq \Delta T$. In a sampling interval, the speed can be considered as constant, and a maximum lag angle $\omega_r \Delta T$ occurs in the current and rotor position that is obtained by the sensor and resolver, respectively. The magnetic field orientation error caused by this delay increases the interfering harmonics energy and deteriorates the control performance, as also mentioned in [7]. The actual system delay time is given in Table I, and the total delay effect is analyzed in two sensorless methods.

B. Delay Influence on Induced HF Current

For the injected square-wave voltage, the delay effect is reflected in two aspects, the envelopes sinusoidal of induced $\alpha\beta$-axis currents is affected by the inverter nonlinearity delay; when the injected frequency is close to the switching frequency, due to calculation delay, the phase of actual induced currents lags behind the ideal signal. Fig. 7 shows the total delay effect when using SWVI, obviously, the envelop of $i_{\alpha h}$ is distorted and its phase is delayed. Under this condition, the square-wave signal in Fig. 2 can be transformed as

$$U^{\hat{r}}_{d\_\mathrm{delay}}(t) = U^{\hat{r}}_{d}(t - \tau_d)\,. \tag{7}$$

Combined with Figs. 2 and 3, due to delay effect, the ideal envelope extraction way can be rewritten as

$$\begin{bmatrix}\Delta i_{\alpha h\_\text{delay}}\\ \Delta i_{\beta h\_\text{delay}}\end{bmatrix}=\frac{U^{\hat{r}}_{d\_\text{delay}}t_m\left(\Delta T,T_h\right)\Delta T}{2(\Sigma L^2-\Delta L^2)}\begin{bmatrix}(\Sigma L-\Delta L)\cos\left(\theta_r-\varphi_{\text{delay}}\right)\\ (\Sigma L-\Delta L)\sin\left(\theta_r-\varphi_{\text{delay}}\right)\end{bmatrix} \tag{8}$$

$$\begin{cases} I_{\cos\_\text{delay}}=\text{sgn}\left(U^{\hat{r}}_{d\_\text{delay}}\right)\Delta i_{\alpha h\_\text{delay}}\\ I_{\sin\_\text{delay}}=\text{sgn}\left(U^{\hat{r}}_{d\_\text{delay}}\right)\Delta i_{\beta h\_\text{delay}}\end{cases} \tag{9}$$

where $\varphi_{\text{delay}}=\hat{\omega}_r\Delta T$; ΣL and ΔL are HF summing-inductance and differential-inductance, respectively; and satisfying $\Sigma L=(L_{dh}+L_{qh})/2$ and $\Delta L=(L_{dh}-L_{qh})/2$.

C. Specialty in NTSMO With Multimode PWM

According to the position demodulation process of NTSMO in [7], by introducing $\alpha\beta$-axis current error, the dynamic equations of the observer can be expressed as

$$\frac{d}{dt}\begin{bmatrix}\tilde{i}_\alpha\\ \tilde{i}_\beta\end{bmatrix}=\boldsymbol{A}\begin{bmatrix}\tilde{i}_\alpha\\ \tilde{i}_\beta\end{bmatrix}+\frac{1}{L_d}\begin{bmatrix}e_\alpha\\ e_\beta\end{bmatrix}+\frac{1}{L_d}\begin{bmatrix}\nu_\alpha\\ \nu_\beta\end{bmatrix} \tag{10}$$

where $\mathbf{A}=\frac{1}{L_d}\begin{bmatrix}-R_s & -\hat{\omega}_r(L_d-L_q)\\ \hat{\omega}_r(L_d-L_q) & -R_s\end{bmatrix}$ R_s, $\boldsymbol{L}_{dq}$, $\boldsymbol{u}_{\alpha\beta}$, and $\boldsymbol{\nu}_{\alpha\beta}$ are, respectively, stator resistance, dq-axis stator inductances, $\alpha\beta$-axis voltages, and $\alpha\beta$-axis control inputs that can be used to estimate extended electromotive force (EEMF).

In asynchronous modulation region, when considering the inverter nonlinearity delay, (10) can be written as

$$\frac{d}{dt}\begin{bmatrix}\tilde{i}_\alpha\\ \tilde{i}_\beta\end{bmatrix}=\boldsymbol{A}\begin{bmatrix}\tilde{i}_\alpha\\ \tilde{i}_\beta\end{bmatrix}+\frac{1}{L_d}\begin{bmatrix}e_{\alpha\_\text{ext}}+U_{\text{err}}D\alpha\\ e_{\beta\_\text{ext}}+U_{\text{err}}D\beta\end{bmatrix}+\frac{1}{L_d}\begin{bmatrix}\nu_\alpha\\ \nu_\beta\end{bmatrix} \tag{11}$$

where $D\alpha$ and $D\beta$ are, respectively, coefficients decided by direction of phase currents, and the following expression can be given:

$$\begin{bmatrix}D\alpha\\ D\beta\end{bmatrix}=\begin{bmatrix}1 & -1 & -1\\ 0 & \sqrt{3} & -\sqrt{3}\end{bmatrix}\times\begin{bmatrix}\text{sgn}\left(i_A\right)\\ \text{sgn}\left(i_B\right)\\ \text{sgn}\left(i_C\right)\end{bmatrix} \tag{12}$$

where $\text{sgn}(x)=\begin{cases}1, x\geq 0\\ -1, x<0\end{cases}$.

During the execution of the sliding mode, the actual $\boldsymbol{\nu}_{\alpha\beta}$ is equal to the summation of EEMF vector and a voltage error vector. Then, the estimated rotor position can be calculated as

$$\hat{\theta}_r=\tan^{-1}\left[-\left(e_{\alpha\_\text{ext}}+U_{\text{err}}D\alpha\right)/\left(e_{\beta\_\text{ext}}+U_{\text{err}}D\beta\right)\right]. \tag{13}$$

Fig. 8 shows the influence of inverter nonlinearity delay on estimated EEMF in asynchronous SVM. At 600 r/min, the $\alpha\beta$-axis voltage errors caused by this delay are presented in Fig. 8(a). Fig. 8(b) shows the comparison of the α-axis estimated EEMF between two cases. Obviously, when considering this delay effect, the fifth and seventh harmonics in $\hat{e}_{\alpha\_\text{ext}}$ are significantly increased, and the waveform also has a certain degree of distortion.

As shown in Fig. 1, a 21-pulse SVM is used in the regular synchronous mode. To illustrate the specificity of inverter delay

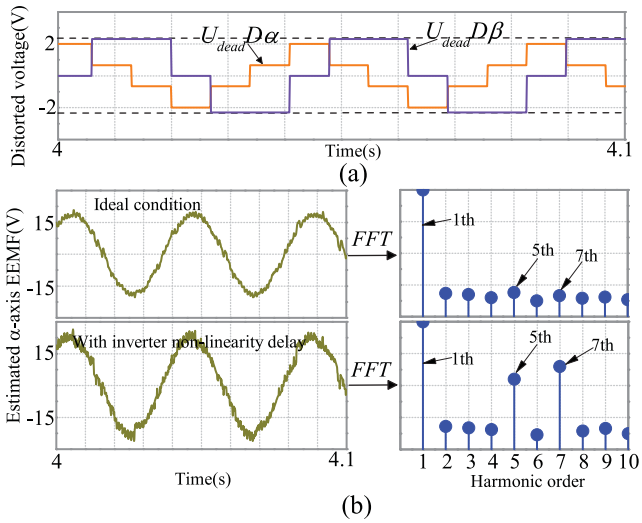

Fig. 8. Influence of inverter nonlinearity delay on estimated EEMF at 600 r/min when using asynchronous SVM. (a) Distorted voltage in the $\alpha\beta$-axis. (b) Estimated α-axis EEMF and FFT analysis.

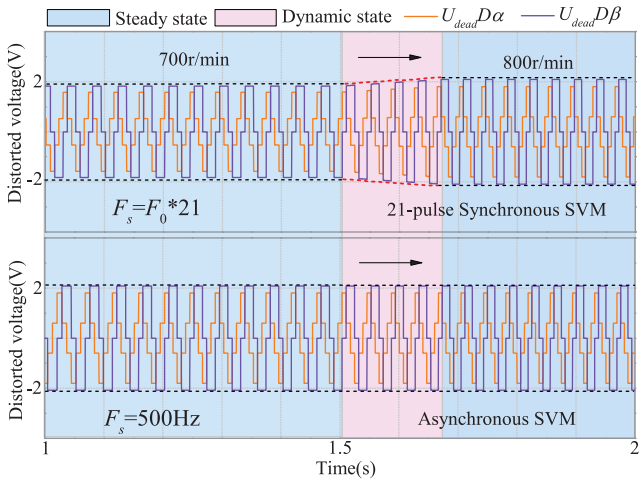

Fig. 9. Comparison of distorted $\alpha\beta$-axis voltages between two PWM modes.

effect in synchronous PWM mode, a distorted voltage comparison is given in Fig. 9. As can be seen, when switching frequency changes, the distorted voltage amplitudes are unequal. Especially in the dynamic state, the distorted $\alpha\beta$-axis voltages in the synchronous modulation mode change continuously. In Fig. 4, the fifth and seventh harmonics in $\hat{\boldsymbol{e}}_{\alpha\beta\_\text{ext}}$ both are converted to sixth pulsation in ε_f through a vector cross-product. So, the error between measured value θ_r and estimated value $\hat{\theta}_r$ in the PLL is a periodically oscillating quantity, whose magnitude is proportional to $U_{\text{dead}}D\alpha\beta$.

When the motor operates in optimal synchronous mode, the calculation delay effect is dominant. For the NTSMO, in the algorithm execution cycle of Fig. 6, the estimated rotor position of kth period is also a delayed signal, and the PWM refresh result is applied to the motor at $(k+1)$th period. On the other hand, according to (10), due to the existence of differentiation,

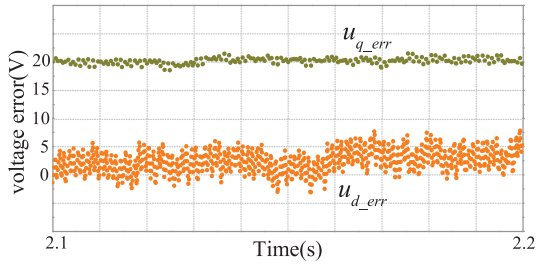

Fig. 10. Voltage errors result from dead-time effect in the dq-axis.

the estimated current used for the calculation is a delayed signal, that is, $\hat{\boldsymbol{i}}_{\alpha\beta}$ lags $\boldsymbol{i}_{\alpha\beta}$ by one ΔT.

IV. Proposed Delay Compensation Method in Multimode Modulation

A. In Carrier-Based PWM Modes

For the inverter nonlinearity delay in carrier-based modulation, in (6), T_{dead} and U_{dc} can be obtained easily, whereas the T_{on} and T_{off} are dependent on operation states, such as dc-bus voltage and phase currents. Therefore, offline measurement of turn-ON and turn-OFF delay is difficult to achieve. Recently, U_{err} is usually calculated online to compensate the VSI nonlinearity in sensorless control [12]. Due to the inverter nonlinearity delay, there is an error between expected and actual values of dq-axis voltages. For IPMSM, MTPA control is usually used. Here, δ is defined as the angle between current vector and q-axis in synchronous reference frame. When δ is small, u_d fluctuates near the zero in MTPA mode. Under this condition, the calculated u_{d_err} also fluctuates around zero, which is not appropriate to the observation of compensation time, as shown in Fig. 10, where $\boldsymbol{u}_{dq\_\text{err}} = \boldsymbol{u}^*_{dq} - \boldsymbol{u}_{dq}$. Therefore, the q-axis voltage error is selected as used original item. As speed increases, the voltage error caused by calculation delay also needs to be considered. Because the maximum calculation delay is one ΔT, regardless of whether the sampling point coincides with the PWM output point, if the current value of $(k+1)$th period can be obtained in kth period, the voltage error caused by the calculation delay can be eliminated. Let $\boldsymbol{i}_{dq\_\text{err}} = \boldsymbol{i}^*_{dq} - \boldsymbol{i}_{dq}$, the basic q-axis voltage and its error can be expressed as

$$u_q = R_s i_q + L_q \frac{di_q}{dt} + L_d \omega_r i_d + \omega_r \psi_f \tag{14}$$

$$u_{q\_\text{err}} = (R_s + L_q D)\, i_{q\_\text{err}} + \omega_r L_d i_{d\_\text{err}}. \tag{15}$$

Then, in sensorless control, the Euler method is used to obtain the following discrete time model, which can provide a simpler model without introducing any unwanted additional nonlinear terms

$$\begin{aligned} i_d(k+1) = &\left(1 - \Delta T \frac{R_{so}}{L_{do}}\right) i_d(k) \\ &+ \Delta T \frac{L_{qo}}{L_{do}} \hat{\omega}_r(k) i_q(k) + \frac{\Delta T}{L_{do}} u_d(k) \end{aligned} \tag{16}$$

$$i_q(k+1) = \left(1 - \Delta T \frac{R_{so}}{L_{qo}}\right) i_q(k) - \Delta T \frac{L_{do}}{L_{qo}} \hat{\omega}_r(k) i_d(k)$$

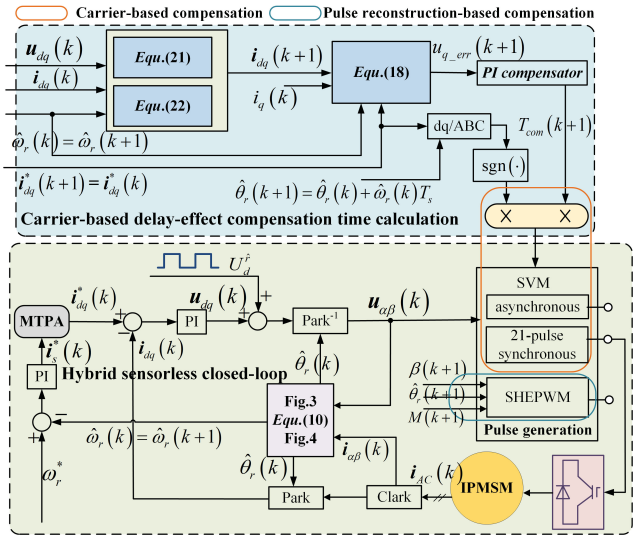

Fig. 11. Whole sensorless control system diagram with the proposed dead-time effect compensation method.

$$-\Delta T \frac{\psi_{fo}}{L_{qo}} \hat{\omega}_r(k) + \frac{\Delta T}{L_{qo}} u_q(k) \tag{17}$$

where subscript "o" represents the used parameters in prediction equation, which are same as the values in Table I. Here, since the mechanical time constant is much larger than the electrical time constant, in a ΔT, $\hat{\omega}_r(k+1)$ can be considered as equivalent to $\hat{\omega}_r(k)$, based on (15), from k to $k+1$, the discretized form of the needed q-axis voltage error can also be obtained as

$$\begin{aligned} u_{q\_\text{err}}(k+1) = R_{so} i_{q\_\text{err}}(k+1) + \frac{L_{qo}}{\Delta T} [i_{q\_\text{err}}(k+1) \\ - i_{q\_\text{err}}(k)] + \hat{\omega}_r(k+1) L_{do} i_{d\_\text{err}}(k+1). \end{aligned} \tag{18}$$

The diagram of delay-compensation-based hybrid IPMSM sensorless control is shown in Fig. 11, and the proposed strategy includes two parts: carrier-based compensation and pulse reconstruction based compensation, and a PI compensator is used in the former. Obviously, the former strategy eliminates the influence of total system delay by compensating the IGBT turn-ON time. The purpose is to calculate the compensation time in carrier-based modulation, and the method itself does not participate in the current closed-loop.

On the other hand, the noise interference of the hardware circuit and the system delay cause zero current clamping, and the actual current repeatedly traverses around the zero point, which makes the current direction near the zero-crossing point difficult to determine. If the compensation is made under a misjudgment of the current direction, the system delay effect is further deteriorated. Here, when the time synchronization can be guaranteed, the three-phase given currents, that is, $\boldsymbol{i}^*_{ABC}(k+1)$, are used to judge the current direction through $\text{sgn}(\cdot)$ function. So, the influence caused by the zero current clamping is successfully avoided. For the PWM generator, the two modulation strategies both are based on carrier, the detailed implementation process

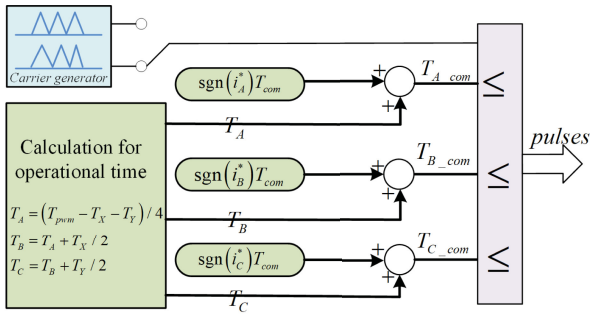

Fig. 12. Compensated PWM generator.

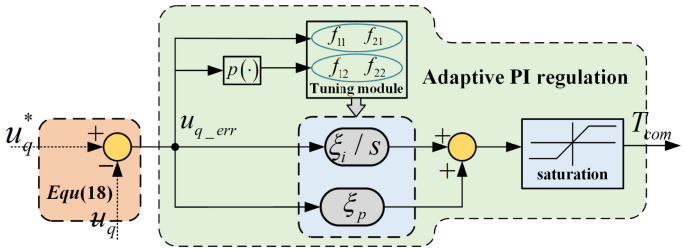

Fig. 13. Design of PI for dead-time compensation.

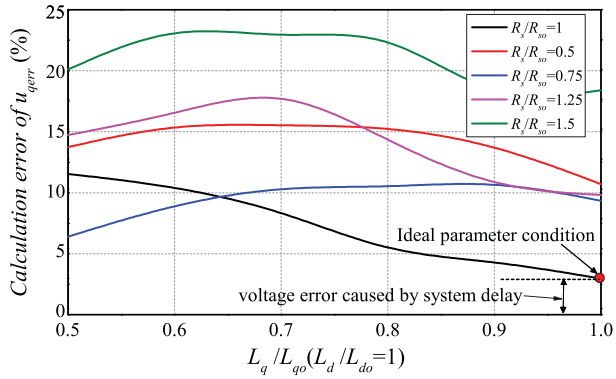

Fig. 14. Calculation error of u_{q_err} with mismatched R_s and L_q at 600 r/min.

with compensation time is shown in Fig. 12, where T_X and T_Y represent the action time of two effective vectors in one carrier period.

As can be seen from Fig. 11, q-axis voltage error $u_{q\_\mathrm{err}}(k+1)$ and parameters of PI compensator together determine the calculation accuracy of $T_{\mathrm{com}}(k+1)$, that is, affecting the result of delay-effect compensation. In the current prediction equations in (16) and (17), the ideal parameters of the IPMSM, including R_s, L_d, and L_q, are required.

According to the conventional prediction control, the current PI regulators are replaced by voltage prediction model, as described in [24], when the actual inductance value differs from the value in the model by more than two times, the system is no longer stable. But, for the PI compensator in the proposed method, the changes in inductance only affect the input value of q-axis voltage error.

Fig. 13 shows the PI compensator design process, the limit range of saturation module is determined by the system delay, through this way, the larger compensation-time estimation error caused by the disturbance is avoided, and the stability of the system can be ensured. Based on this, in order to make the calculated compensation-time T_{com} has better dynamic response without steady-state error, an online adaptive method is used to correct the proportional and integral coefficients, voltage error u_{q_err} and its changing rate $p(u_{q\_\mathrm{err}})$ are selected as inputs to the PI parameter adaptive tuning module. Then, the gains can be expressed as

$$\begin{cases} \xi_p = f_1\left(u_{q\_\mathrm{err}}, pu_{q\_\mathrm{err}}\right) = f_{11}\left(u_{q\_\mathrm{err}}\right) + f_{12}\left(pu_{q\_\mathrm{err}}\right) \\ \xi_i = f_2\left(u_{q\_\mathrm{err}}, pu_{q\_\mathrm{err}}\right) = f_{21}\left(u_{q\_\mathrm{err}}\right) + f_{22}\left(pu_{q\_\mathrm{err}}\right). \end{cases} \tag{19}$$

The tuning module is presented as

$$\begin{cases} f_{11}\left(u_{q\_\mathrm{err}}\right) = k_{11}[1-\exp(-(u_{q\_\mathrm{err}}/b_{11})^2)] \\ f_{21}\left(u_{q\_\mathrm{err}}\right) = k_{21}[1-\exp(-(u_{q\_\mathrm{err}}/b_{21})^2)] \\ f_{12}\left(u_{q\_\mathrm{err}}\right) = k_{12}\exp(-(pu_{q\_\mathrm{err}}/b_{12})^2) \\ f_{22}\left(u_{q\_\mathrm{err}}\right) = k_{22}\exp(-(pu_{q\_\mathrm{err}}/b_{22})^2) \end{cases} \tag{20}$$

where k_{11}, k_{21}, k_{12}, and k_{22} are scale factors, which can adjust the ratio of u_{q_err} and pu_{q_err} microscopically. b_{11}, b_{21}, b_{12}, and b_{22} are weighting factors, which can be used to correct the weight of u_{q_err} and pu_{q_err} from a small amount. Here, $k_{11}=k_{12}=5$, $k_{21}=k_{22}=1$, and $b_{11}=b_{21}=b_{12}=b_{22}=2$. By self-tuning the PI gains, when u_{q_err} is large, the larger ξ_p accelerates the response rate, but does not produce excessive overshoot. When ξ_p enters a small range, it can guarantee steady-state accuracy. For ξ_i, in the initial response stage, the smaller ξ_i can avoid integral saturation, and as u_{q_err} and pu_{q_err} decrease, ξ_i increases appropriately.

Through aforementioned analysis, the saturation module can ensure that the compensation value is within a stable range, and the adaptive PI adjustment enhances the dynamic response capability of the compensation time in calculation process. When the used R_{so}, L_{do}, and L_{qo} in the prediction equation deviate from the actual values, the calculated q-axis voltage error does not accurately reflect the system delay effect. When i_q is small, the q-axis magnetic circuit is not saturated, and L_q can be considered as a constant. As the load increases, the q-axis magnetic circuit becomes saturated and L_q decreases. According to the variation law of i_q and i_d in the MTPA mode, when the HF signal is not injected into the d-axis, i_d increases negatively as the load increases. Under injection condition, the IPMSM relies on structure saliency whose d-axis magnetic circuit does not need to be saturated. Then, in the entire carrier-based modulation region, L_d can be regarded as a constant. Fig. 14 shows the q-axis voltage error ratio when actual R_s and L_q change. Obviously, the mismatch between actual and used parameters increases the q-axis voltage error, then the compensation time is not accurate. In order to reduce the influence of motor parameters mismatch on the delay compensation, a current weighting method is used

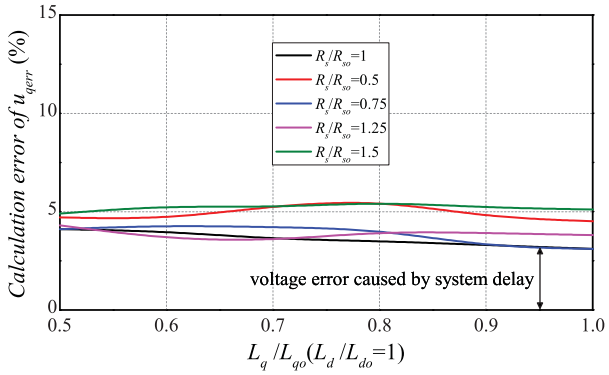

Fig. 15. u_{q_err} with mismatched R_s and L_q after using robust current prediction equation.

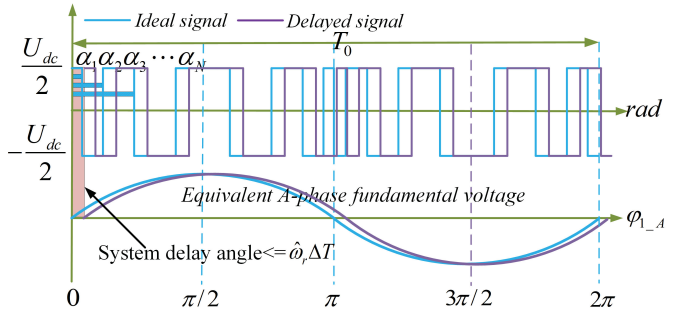

Fig. 16. *A*-phase voltage pulse reconstruction under system delay.

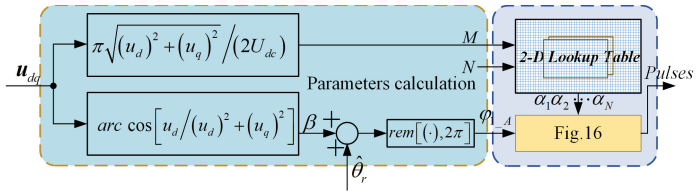

Fig. 17. Implementation process of SHEPWM.

in the prediction equation, (16) and (17) can be transformed as

$$i_d(k+1) = \left(1 - \Delta T\frac{R_{so}}{L_{do}}\right)\left[mi_d^*(k) + ni_d(k)\right] + \Delta T\frac{L_{qo}}{L_{do}}\hat{\omega}_r(k)\left[mi_q^*(k) + ni_q(k)\right] + \frac{\Delta T}{L_{do}}u_d(k) \tag{21}$$

$$i_q(k+1) = \left(1 - \Delta T\frac{R_{so}}{L_{qo}}\right)\left[mi_q^*(k) + ni_q(k)\right] - \Delta T\frac{L_{do}}{L_{qo}}\hat{\omega}_e(n)\left[mi_d^*(k) + ni_d(k)\right] - \Delta T\frac{\psi_{fo}}{L_{qo}}\hat{\omega}_r(k) + \frac{\Delta T_s}{L_{qo}}u_q(k) \tag{22}$$

where m and n are weighting factors, satisfying $m + n = 1$. As n decreases, the calculated voltage error is more robust to parameter changes, and the weighting factor can be selected by online adjustment, here, $m = 0.8$ and $n = 0.2$. Fig. 15 shows the u_{q_err} variation after using the robust current prediction equation, as can be seen, by introducing weighting way, u_{q_err} can be controlled within 5%. Based on this, the influence of motor parameter mismatch on the accuracy of compensation time calculation is greatly weakened, then the system delay compensation has a better effect.

Overall, the proposed robust current prediction method is used to eliminate the influence of motor parameters mismatch. The proposed adaptive tuning module and saturation module in PI compensator together guarantee the accuracy and stability of the compensation.

B. In SHEPWM

As described in [18], the principle of SHEPWM techniques is based on decomposition of the PWM voltage using Fourier theory, and merely depends on the formulation of the given waveform and its properties. Fig. 16 shows the pulse reconstruction way in SHEPWM, where T_0 is fundamental voltage period, N is the number of switching angles in one-fourth fundamental period and the angle value satisfies $\alpha_1 < \alpha_2 < \cdots < \alpha_N$. Because this modulation does not depend on the carrier, the delay compensation method needs to be redesigned. Fig. 17 shows the implementation process of SHEPWM, where M is modulation depth that determine the output voltage amplitude, β is voltage vector angle in the dq-axis, and φ_{1_A} is voltage vector angle in ABC-coordinates. As can be seen, in SHEPWM, the PWM output is selected as the end point of a fundamental voltage period, so, the system delay is less than or equal to ΔT. By controlling the selection accuracy of M, the influence of system delay on the switching angle α_N selection can be neglected, so, $M(k+1) = M(k)$. Here, in the process of solving the switching angle equation, the resolution of M is 0.01. In kth period, if φ_{1_A} of $(k+1)$th period can be obtained, the delay effect can be eliminated. According to Fig. 17, for φ_{1_A}, $\hat{\omega}_r$ is constant in a sampling interval, $\varphi_{1\_A}(k+1)$ can be calculated by adding $\beta(k+1)$ and $\hat{\theta}_r(k+1)$. The following relationship can be used:

$$\begin{cases} \beta(k+1) = \beta(k) + \hat{\omega}_r(k)\Delta T \\ \hat{\theta}_r(k+1) = \hat{\theta}_r(k) + \hat{\omega}_r(k)\Delta T. \end{cases} \tag{23}$$

C. Compensation Analysis in Sensorless Performance

In the hybrid sensorless control, the fusion input error ε_H is used to estimate position and speed in Fig. 4. On the other hand, due to the use of PLL, the performance of sensorless dynamic state that includes disturbance and transition zone can also be reflected by this input error. When ε_H is controlled near zero, the estimated rotor position is equal to the calculated value, then the corresponding position estimation error is also minimum. The transition between SWVI and NTSMO for position estimation is achieved in asynchronous SVM modulation, which is combined with calculation-time-based compensation. When the inverter

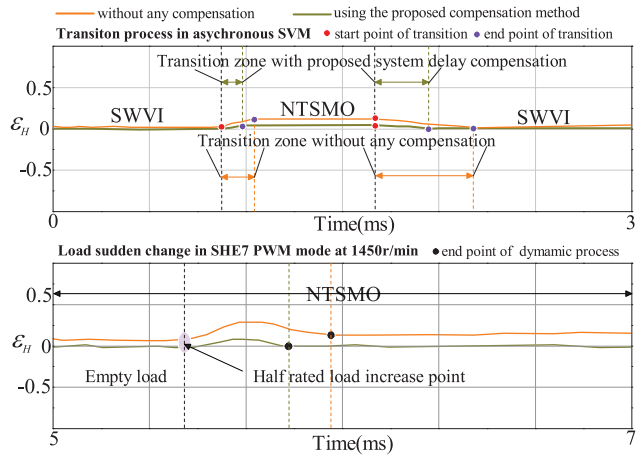

Fig. 18. Comparison of dynamic region performance between uncompensated and compensated signal.

operates in the selective harmonic elimination (SHE) region, the prediction equation is used to eliminate the delay effect. Fig. 18 shows the simulation comparison of ε_H between uncompensated and compensated condition, where the delay-time parameters are listed in Table I.

In Fig. 18, the transition zone between SWVI and NTSMO belongs to a speed change region, and a hybrid position observer is used according to both ω_{sd} and ω_{su} in Fig. 4. Due to the magnetic orientation error caused by system delay, there is a longer duration of the transition region, and the larger ε_H occurs in dynamic process without compensation strategy. Considering the dynamic response caused by load sudden change, ε_H needs longer time to reach steady state without compensation. In contrast, when proposed system delay compensation is adopted, ε_H can be controlled near zero irrespective of operation conditions.

Besides, the current harmonic energy distribution can be used to evaluate sensorless closed-loop performance as well. In the hybrid sensorless control, high frequency injection (HFI) introduces additional noise signals. When the switching frequency is reduced, the injected voltage error caused by the system delay further exacerbates the noise harmonics. As the fundamental frequency increases, the back EMF method faces the problem that coupling effect of *dq*-axis currents. Meanwhile, the magnetic field orientation error caused by the delay also brings more harmonic energy interference. In multimode PWM, in order to analyze the influence of proposed delay-compensation on the harmonic noise energy, the power spectral density (PSD) in [7] is selected as the evaluation index.

Fig. 19 shows the current PSD comparison in multimode PWM. When using SWVI in asynchronous SVM, PSD of the induced HF current is mainly concentrated on the HF signal and its low-odd-order harmonics. In this modulation range, the influence of inverter nonlinearity delay is still obvious. Without compensation, there is a large PSD amplitude at the third, fifth, and seventh harmonics. With delay compensation, the noise energy of the fifth and seventh harmonics is significantly suppressed, similar phenomenon exists in fundamental current when using NTSMO under asynchronous SVM. In this high-speed range, the influence of the inverter nonlinearity delay can be neglected, and the calculation delay plays a major role. Obviously, the proposed system delay compensation can eliminate the interference harmonic energy significantly.

V. Experimental Results and Discussions

In this article, based on RT-LAB controller, the proposed sensorless strategy has been verified at a 3.7-kW IPMSM platform, as shown in Fig. 20. The major parameters under the test are listed in Table II. The control performance of the system delay compensation method in different PWM modes is shown in this section, consistent with the speed range in Fig. 1. All the following experimental waveforms are achieved with the IPMSM operating at sensorless control, and the condition is divided into steady state and dynamic state.

A. Steady-State Performance

Fig. 21 shows the experimental results for the identification of T_{com} at various steady operating points. In the experimental setup, a magnetic powder brake is utilized as load system. As can be seen, the identified T_{com} tends to increase with decreasing rotor speed. On the other hand, T_{com} increases with the increase rms of phase current. Under this compensation condition, the currents and position estimation performance are compared in different PWM modes.

Fig. 22 shows the waveforms of induced α-axis HF current and PSD distribution at 100 r/min with rated load. In Fig. 22(a), without any compensation, the current envelop has obvious burr and its sinusoidal performance is deteriorated. Meanwhile, due to the system delay, a large phase lag appears in HF current. After compensation, the current delay is eliminated, and envelop is smoother. From the PSD comparison of *A*-phase current in Fig. 22(b), with the proposed method, the energy of odd-order harmonics in HF component is significantly weakened, especially in third, fifth, and seventh harmonics. So, in this speed region, inverter nonlinearity delay has a greater influence weight, the compensation has a good elimination effect on this delay.

Fig. 23 shows the waveforms of fundamental current and its PSD in half-rated load condition, the given speed is set as 700 r/min. Before delay compensation, the *A*-phase current is distorted and has a phase lag. When using proposed method, the current performance is optimized obviously. From PSD distribution, under the 21-pulse synchronous modulation, the noise energy is mainly concentrated in the seventeenth and nineteenth harmonics. After delay compensation, the PSD of each harmonic is obviously suppressed, especially in 408 and 456 Hz, and the harmonic performance is optimized overall. In order to verify the effectiveness of delay compensation in SHE modulation mode, the current performance comparison is given under 1500 r/min, as shown in Fig. 24. Obviously, the phase current is distorted and has a large lag when the delay effect is not compensated, meanwhile, the coupling term is affected by the delay, and the *dq*-axis current also has a large oscillation. After compensation, due to the elimination of delay influence, the sinusoidal and tracking of the current can effectively guaranteed. For the PSD in SHE7, the low-order harmonics energy is eliminated. In

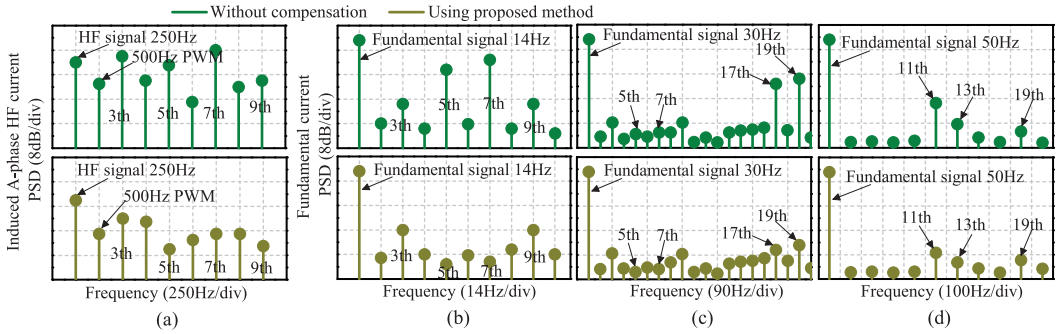

Fig. 19. Current PSD analysis in sensorless control with multimode modulation. (a) SWVI in asynchronous SVM. (b) NTSMO in asynchronous SVPWM. (c) NTSMO in 21-pulse synchronous SVM. (d) NTSMO in 7-pulse SHEPWM.

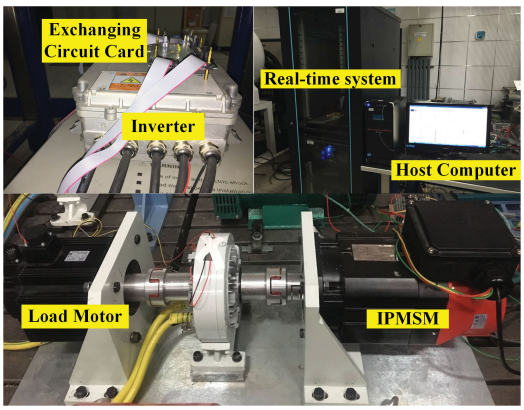

Fig. 20. Experimental test setup of 3.7-kW IPMSM drive.

TABLE II
IPMSM PARAMETERS

Quantity	Value$[Unit]$
Rated Power	$3.7[kW]$
Rated Torque	$17.7[Nm]$
Rated Current	$14[A]$
Rated Speed	$2000[rpm]$
DC Link Voltage	$270[V]$
Stator Resistance	0.55Ω
Stator Inductance	$L_d = 6.6[mH], L_q = 14.3[mH]$
Overall Inertia	$3.94e-3[kg \cdot m^2]$

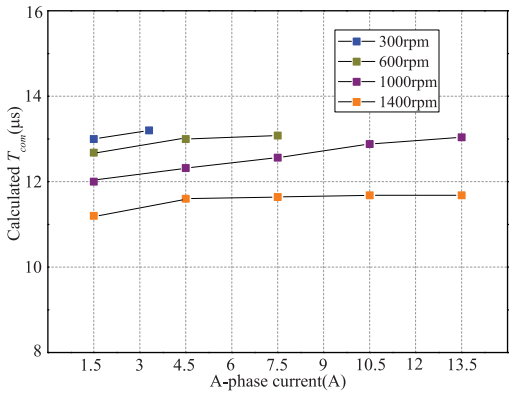

Fig. 21. Experimental result for the identification of T_{com} at various steady operating points.

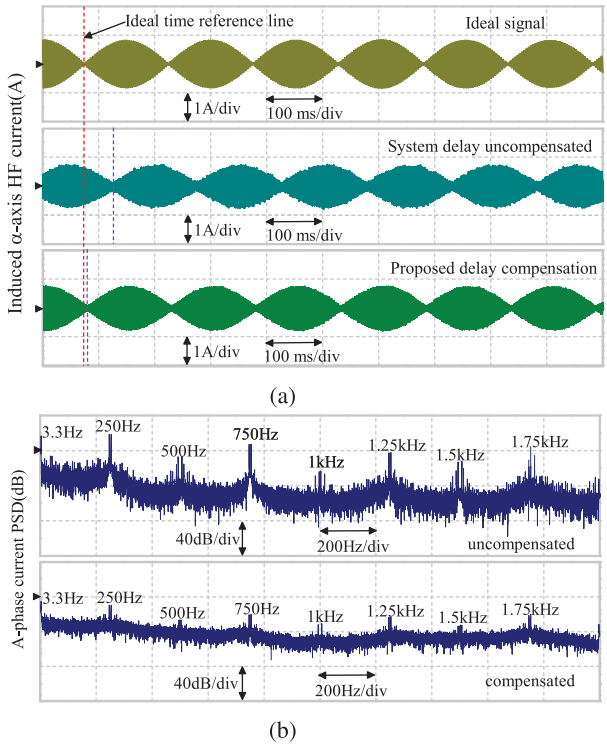

Fig. 22. HF current performance comparison with rated load when using SWVI at 100 r/min. (a) Induced α-axis current. (b) PSD distribution.

PSD of eleventh, thirteenth, and nineteenth harmonics, after compensation, the corresponding energies all are reduced, and the PSD distribution is also smoother.

Fig. 25 shows the position estimation performance comparison at 700 r/min, when using NTSMO in 21-pulse synchronous modulation, the inherent calculation delay of the system is not very obvious. As can be seen, before compensation, there is a slight lag in estimated position, however, due to the existence of inverter nonlinearity delay, the position estimation error still has large fluctuations. After using delay compensation, the estimated signals all are optimized.

Fig. 26 shows the position estimation performance at 1500 r/min when using SHE7 modulation mode. In the running state without delay compensation, the estimated speed has large

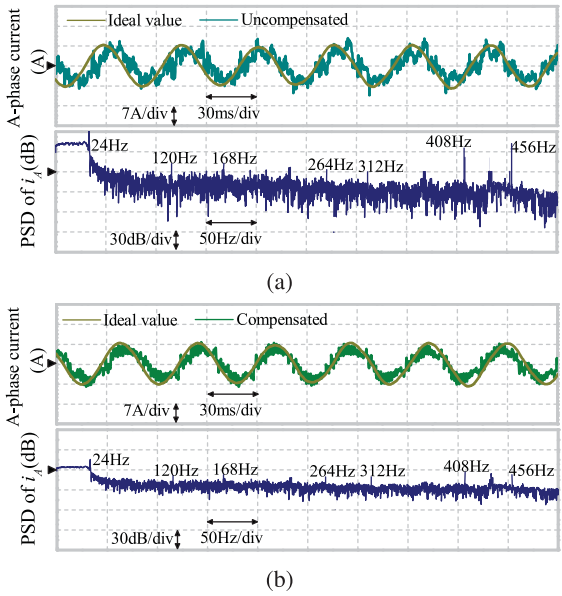

Fig. 23. *A*-phase current performance comparison with half-rated load when using NTSMO in 21-pulse syn-modulation (700 r/min). (a) Uncompensated. (b) Compensated.

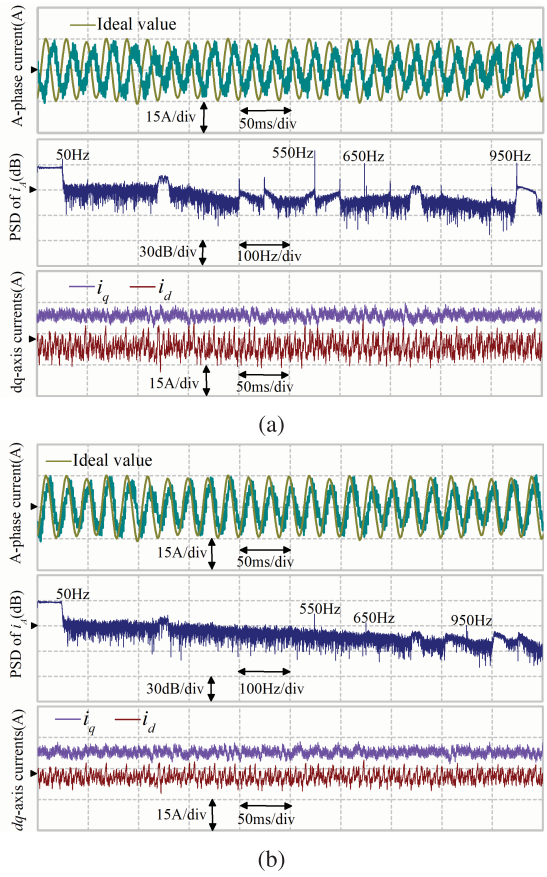

Fig. 24. Current performance comparison with rated load when using NTSMO in SHE7 (1500 r/min). (a) Uncompensated. (b) Compensated.

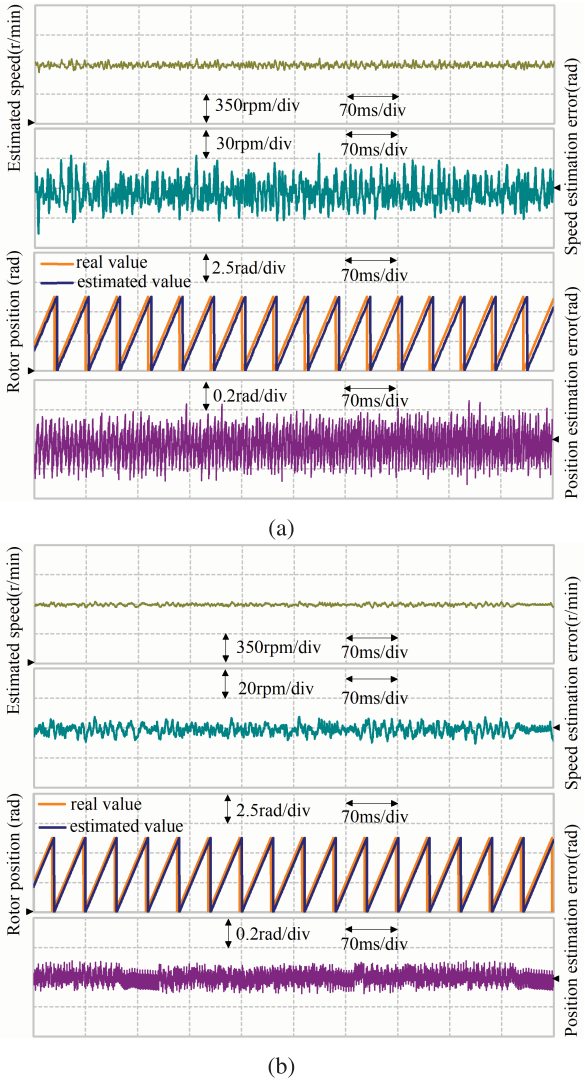

Fig. 25. Position estimation performance comparison with rated load when using NTSMO in 21-pulse syn-modulation (700 r/min). (a) Uncompensated. (b) Compensated.

fluctuations, and the average fluctuation amplitude can reach 150 r/min, which means that in the high-speed region, the existence of the system delay increases the current oscillation, and causes speed fluctuations, which is also the embodiment of the gradual deterioration of the sensorless closed-loop performance. Meanwhile, the estimated position is also distorted, and the maximum error exceeds 0.3 rad. After using proposed method, the estimated position lag is eliminated obviously, and the position estimation error is also reduced.

B. Dynamic State Performance

In order to evaluate the dynamic response of the adaptive PI compensator in the calculation process, Fig. 27 shows the response comparison of speed change between two PI structure. For the adaptive one, the parameters are designed as Fig. 13.

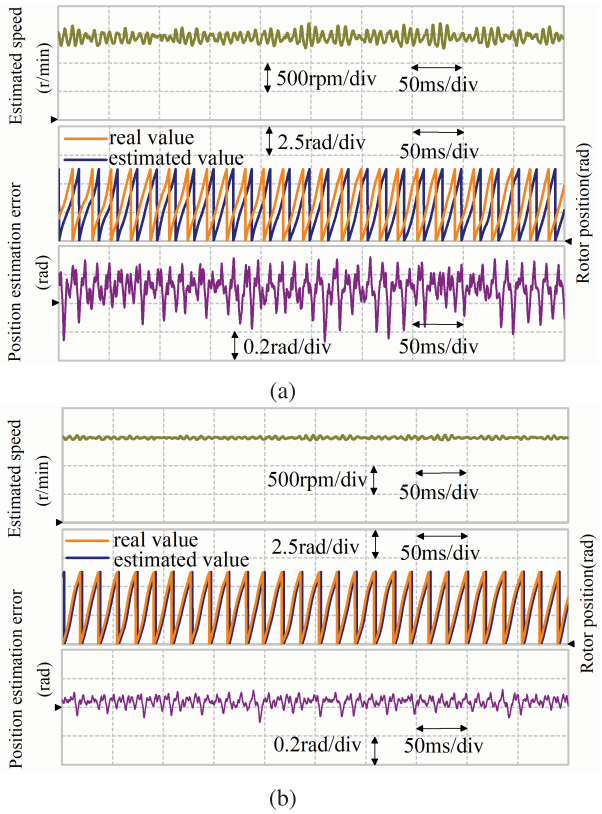

Fig. 26. Position estimation performance comparison with rated load when using NTSMO in 7-pulse SHEPWM (1500 r/min). (a) Uncompensated. (b) Compensated.

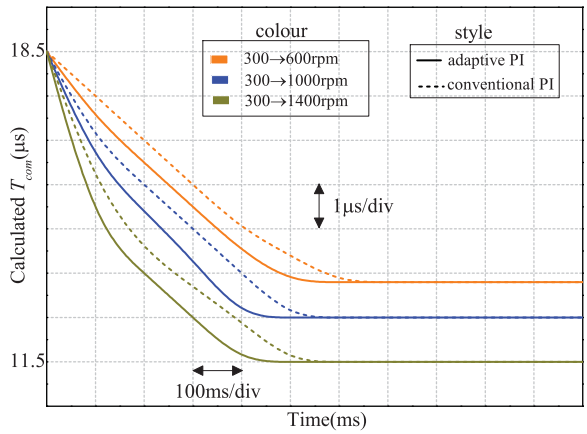

Fig. 27. Speed response comparison of calculated T_{com} between adaptive and conventional PI.

In conventional PI, the proportional and integral coefficients are 5 and 1, respectively. Obviously, when using the adaptive structure, as motor speed increases, the compensation time T_{com} can reach a stable value faster. Then, based on this PI, the dynamic position estimation performance is tested.

For the hybrid position observer, it is also necessary to evaluate the dynamic performance of the transition zone, where the upper and lower limits of the speed are selected as 150 and

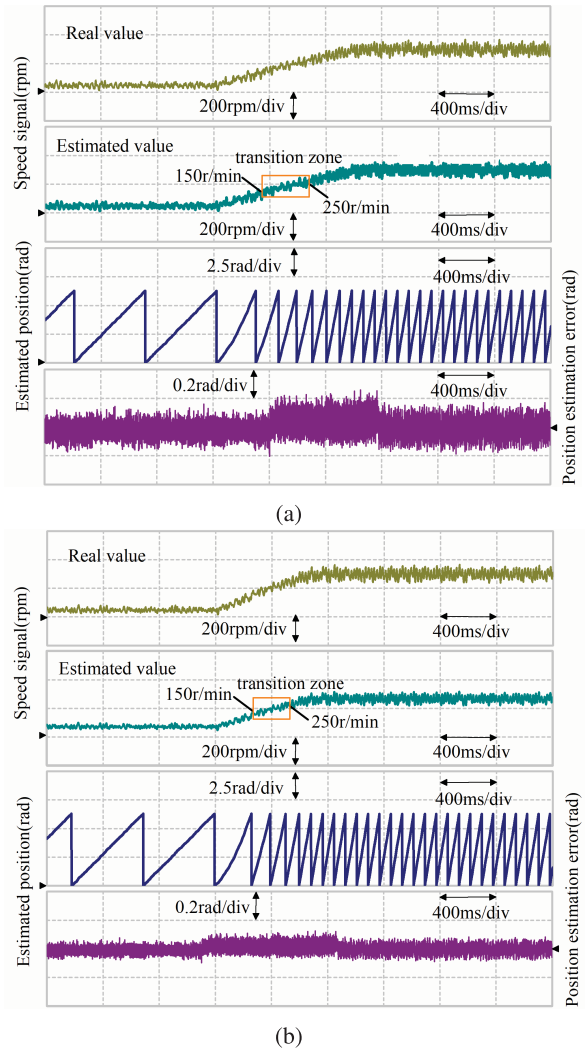

Fig. 28. Position estimation performance comparison with rated load in hybrid position observer (50 r/min→300 r/min). (a) Uncompensated. (b) Compensated.

250 r/min, respectively, as presented in Fig. 28. Under rated load, the speed range is 50 to 300 r/min, it can be seen that the transition time of the two sensorless methods is significantly shortened after the delay compensation. In the entire transition process, the position estimation error can be controlled within 0.1 rad when using proposed method.

Considering load disturbance, the load sudden increase condition is 1 to 10 N·m, the process of sudden load release is the opposite. Fig. 29 shows the performance comparison of position estimation when using SWVI under torque disturbance, the steady speed is set as 30 r/min. As can be seen, after system delay compensation, the response rate of estimated speed and q-axis current both are significantly improved when faces load disturbance, and the position estimation error can be controlled within 0.1 rad in entire process. In Fig. 30, the SHE7 mode is used, and the estimation performance of NTSMO at 1400 r/min is given, obviously, without compensation, when load disturbance occurs, there is greater estimated speed fluctuations, and the maximum position estimation error reaches 0.3 rad. After

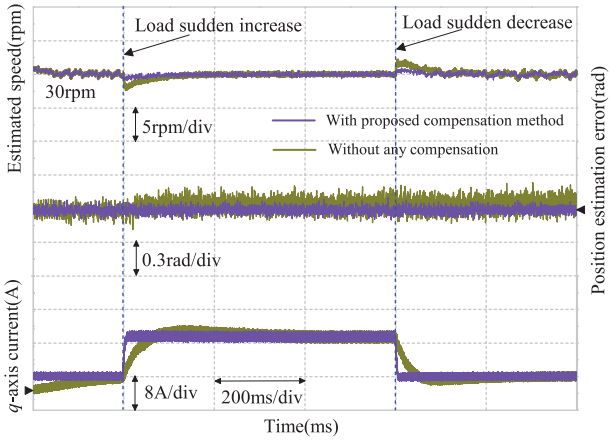

Fig. 29. Position estimation performance comparison with load disturbance when using SWVI (30 r/min).

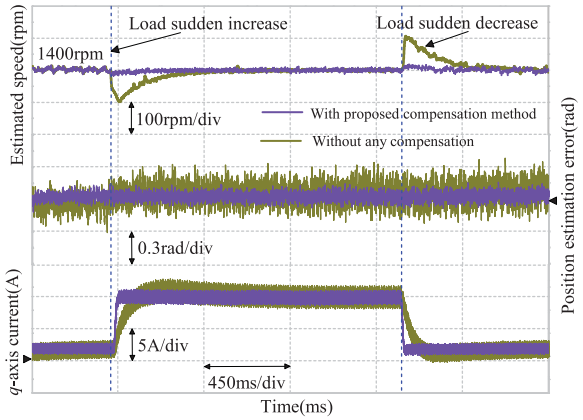

Fig. 30. Position estimation performance comparison with load disturbance when using NTSMO (1400 r/min).

using prediction compensation equation as (23), the dynamic response and position estimation accuracy have been optimized.

VI. Conclusion

For the rail transit application, a hybrid position observer with an overall system delay compensation method in multimode PWM has been proposed for IPMSM sensorless drives. The influence mechanism of the system delay in square wave injection and NTSMO is analyzed. When the inverter works in asynchronous modulation or 21-pulse synchronous modulation, the q-axis voltage error is used to estimate the compensation time value. Considering the existence of calculation delay, the Euler prediction theory is used in the voltage error calculation, and finally a system delay elimination strategy for compensating the IGBT three-phase turn-ON time is designed. When inverter enters SHEPWM mode, the voltage vector angle and the rotor position angle are calculated by a simple prediction way, and the influence of calculation delay is eliminated when the PWM pulse is reconstructed. The proposed method is not restricted in the rail transit application and it can be applied also in other areas where multimode PWM and sensorless control are required. The whole sensorless performance is verified on a 3.7-kW IPMSM platform.

References

[1] C. Wang, K. Wang, and X. You, "Research on synchronized SVPWM strategies under low switching frequency for six-phase VSI-fed asymmetrical dual stator induction machine," *IEEE Trans. Ind. Electron.*, vol. 63, no. 11, pp. 6767–6776, Nov. 2016.

[2] H. Yang, Y. Zhang, G. Yuan, P. D. Walker, and N. Zhang, "Hybrid synchronized PWM schemes for closed-loop current control of high-power motor drives," *IEEE Trans. Ind. Electron.*, vol. 64, no. 9, pp. 6920–6929, Sep. 2017.

[3] G. Wang, J. Kuang, N. Zhao, G. Zhang, and D. Xu, "Rotor position estimation of PMSM in low-speed region and standstill using zero-voltage vector injection," *IEEE Trans. Power Electron.*, vol. 33, no. 9, pp. 7948–7958, Sep. 2018.

[4] G. Andreescu, C. I. Pitic, F. Blaabjerg, and I. Boldea, "Combined flux observer with signal injection enhancement for wide speed range sensorless direct torque control of IPMSM drives," *IEEE Trans. Energy Conver.*, vol. 23, no. 2, pp. 393–402, Jun. 2008.

[5] Z. Chen, H. Zhang, W. Tu, G. Luo, D. Manoharan, and R. Kennel, "Sensorless control for permanent magnet synchronous motor in rail transit application using segmented synchronous modulation," *IEEE Access*, vol. 7, pp. 76669–76679, 2019.

[6] X. Ding *et al.*, "Analytical and experimental evaluation of SiC-inverter nonlinearities for traction drives used in electric vehicles," *IEEE Trans. Veh. Technol.*, vol. 67, no. 1, pp. 146–159, Jan. 2018.

[7] H. Zhang *et al.*, "A time-delay compensation method for IPMSM hybrid sensorless drives in rail transit applications," *IEEE Trans. Ind. Electron.*, vol. 66, no. 9, pp. 6715–6726, Sep. 2019.

[8] J. M. Guerrero, M. Leetmaa, F. Briz, A. Zamarron, and R. D. Lorenz, "Inverter nonlinearity effects in high-frequency signal-injection-based sensorless control methods," *IEEE Trans. Ind. Appl.*, vol. 41, no. 2, pp. 618–626, Mar./Apr. 2005.

[9] D. Kim, Y. Kwon, S. Sul, J. Kim, and R. Yu, "Suppression of injection voltage disturbance for high-frequency square-wave injection sensorless drive with regulation of induced high-frequency current ripple," *IEEE Trans. Ind. Appl.*, vol. 52, no. 1, pp. 302–312, Jan./Feb. 2016.

[10] D. E. Salt, D. Drury, D. Holliday, A. Griffo, P. Sangha, and A. Dinu, "Compensation of inverter nonlinear distortion effects for signal-injection-based sensorless control," *IEEE Trans. Ind. Appl.*, vol. 47, no. 5, pp. 2084–2092, Sep./Oct. 2011.

[11] G. Wang, H. Zhan, G. Zhang, X. Gui, and D. Xu, "Adaptive compensation method of position estimation harmonic error for EMF-based observer in sensorless IPMSM drives," *IEEE Trans. Power Electron.*, vol. 29, no. 6, pp. 3055–3064, Jun. 2014.

[12] D. Liang, J. Li, R. Qu, and W. Kong, "Adaptive second-order sliding-mode observer for PMSM sensorless control considering VSI nonlinearity," *IEEE Trans. Power Electron.*, vol. 33, no. 10, pp. 8994–9004, Oct. 2018.

[13] G. Wang, L. Yang, B. Yuan, B. Wang, G. Zhang, and D. Xu, "Pseudo-random high-frequency square-wave voltage injection based sensorless control of IPMSM drives for audible noise reduction," *IEEE Trans. Ind. Electron.*, vol. 63, no. 12, pp. 7423–7433, Dec. 2016.

[14] Q. P. Tang, A. Shen, X. Luo, and J. Xu, "PMSM sensorless control by injecting HF pulsating carrier signal into ABC frame," *IEEE Trans. Power Electron.*, vol. 32, no. 5, pp. 3767–3776, May 2017.

[15] C. Gong, Y. Hu, J. Gao, Y. Wang, and L. Yan, "An improved delay-suppressed sliding-mode observer for sensorless vector-controlled PMSM," *IEEE Trans. Ind. Electron.*, vol. 67, no. 7, pp. 5913–5923, Jul. 2020.

[16] S. Yang and G. Chen, "High-speed position-sensorless drive of permanent-magnet machine using discrete-time EMF estimation," *IEEE Trans. Ind. Electron.*, vol. 64, no. 6, pp. 4444–4453, Jun. 2017.

[17] H. Zhang, W. Liu, Z. Chen, and N. Jiao, "Smooth transition of multimode synchronous modulation for IPMSM sensorless drives in rail-transit applications," *IEEE Trans. Ind. Electron.*, to be published.

[18] M. S. A. Dahidah, G. Konstantinou, and V. G. Agelidis, "A review of multilevel selective harmonic elimination PWM: Formulations, solving algorithms, implementation and applications," *IEEE Trans. Power Electron.*, vol. 30, no. 8, pp. 4091–4106, Aug. 2015.

[19] A. Yousefi-Talouki, P. Pescetto, G. Pellegrino, and I. Boldea, "Combined active flux and high-frequency injection methods for sensorless direct-flux vector control of synchronous reluctance machines," *IEEE Trans. Power Electron.*, vol. 33, no. 3, pp. 2447–2457, Mar. 2018.

[20] M. Seilmeier and B. Piepenbreier, "Sensorless control of PMSM for the whole speed range using two-degree-of-freedom current control and HF test current injection for low-speed range," *IEEE Trans. Power Electron.*, vol. 30, no. 8, pp. 4394–4403, Aug. 2015.
[21] O. Wallmark and L. Harnefors, "Sensorless control of salient PMSM drives in the transition region," *IEEE Trans. Ind. Electron.*, vol. 53, no. 4, pp. 1179–1187, Jun. 2006.
[22] Y. Yoon, S. Sul, S. Morimoto, and K. Ide, "High-bandwidth sensorless algorithm for ac machines based on square-wave-type voltage injection," *IEEE Trans. Ind. Appl.*, vol. 47, no. 3, pp. 1361–1370, May/Jun. 2011.
[23] H. Zhang, W. Liu, Z. Chen, N. Jiao, and D. Zhao, "Comparison analysis of low-switching-frequency-based IPMSM sensorless drives considering regulators, observer and inverter non-linearity," *IET Elect. Power Appl.*, vol. 13, no. 7, pp. 1022–1031, 2019.
[24] J. C. Moreno, J. M. Espi Huerta, R. G. Gil, and S. A. Gonzalez, "A robust predictive current control for three-phase grid-connected inverters," *IEEE Trans. Ind. Electron.*, vol. 56, no. 6, pp. 1993–2004, Jun. 2009.

Hang Zhang (Student Member, IEEE) received the B.S. degree in electronic and information engineering from the Hefei University of Technology, Hefei, China, in 2010, the M.S. degree in detection technique and automatic device from the Xi'an University of Science and Technology, Xi'an, China, in 2013, and the Ph.D. degree in electrical engineering from Northwestern Polytechnical University, Xi'an, China, in 2019.

His research interests include sensorless control and inverter modulation strategy for rail transit permanent magnet synchronous motor drives.

Weiguo Liu (Senior Member, IEEE) received the B.S. degree in electrical machines engineering from the Huazhong University of Science and Technology, Wuhan, China, in 1982, and the M.S. degree in electrical engineering and the Ph.D. degree in control theory and control engineering from Northwestern Polytechnical University, Xi'an, China, in 1988 and 1999, respectively.

He is currently a Professor with the Department of Electrical Engineering, Northwestern Polytechnical University, and a Guest Professor of the University of Federal Defense, Munich, Germany. He is also the Director of the Institute of Rare Earth Permanent Magnet Electrical Machines and Control Technology, Northwestern Polytechnical University. His research interests include brushless dc machines, PM synchronous machines, dc machines, and induction machines.

Dr. Liu was the Chairman of the Organizing Committee of the 32nd Chinese Control Conference, Xi'an, China, in July 2013.

Zhe Chen was born in Huozhou, China, in 1986. He received the B.S. and M.S. degrees from Automation Faculty, Northwestern Polytechnical University (NPU), Xi'an, China, in 2008 and 2011, respectively, and the Dr.-Ing. degree from the Institute for Electrical Drive Systems and Power Electronics, Technical University of Munich, Munich, Germany, in 2016, all in electrical engineering.

Since 2017, he has been an Associate Professor with NPU. His research interests include predictive control and sensorless control for power electronics and electric drives, renewable energy systems, and application of field-programmable gate array based digital controller.

Ningfei Jiao (Member, IEEE) received the B.S. and Ph.D. degrees in electrical engineering from Northwestern Polytechnical University, Xi'an, China, in 2011 and 2017, respectively.

From 2013 to 2014, he was a Visiting Scholar with Michigan Power and Energy Laboratory, University of Michigan, Ann Arbor, MI, USA. He is currently an Associate Researcher with Northwestern Polytechnical University. His research interests include aircraft starter/generator, design, analysis, and control of PMSMs.